



HHS Public Access

Author manuscript

Nat Chem. Author manuscript; available in PMC 2021 December 21.

Published in final edited form as:

Nat Chem. 2021 July ; 13(7): 683–691. doi:10.1038/s41557-021-00705-2.

Metal Ion Fluxes Controlling Amphibian Fertilization

John F. Seeler¹, Ajay Sharma², Nestor J. Zaluzec³, Reiner Bleher⁴, Barry Lai⁵, Emma G. Schultz^{2,6}, Brian M. Hoffman^{1,2}, Carole LaBonne^{1,6,*}, Teresa K. Woodruff^{1,6,7,11,*}, Thomas V. O'Halloran^{1,2,6,8,9,10,*}

¹Department of Molecular Biosciences, Northwestern University, Evanston, IL, USA.

²Department of Chemistry, Northwestern University, Evanston, IL, USA.

³Photon Sciences Directorate, Argonne National Laboratory, Argonne, IL, USA

⁴Department of Materials Science and Engineering, Northwestern University, Evanston, IL, USA.

⁵Advanced Photon Source, Argonne National Laboratory, Argonne, IL, USA.

⁶The Chemistry of Life Processes Institute, Northwestern University, Evanston, IL, USA.

⁷Department of Obstetrics and Gynecology and Northwestern University, Chicago, IL, USA.

⁸Department of Medicine, Feinberg School of Medicine, Northwestern University, Chicago, IL, USA.

⁹Department of Chemistry, Michigan State University, East Lansing, MI, USA.

¹⁰Department of Microbiology and Molecular Genetics, Michigan State University, East Lansing, MI, USA.

¹¹Department of Obstetrics and Gynecology, Michigan State University, East Lansing, MI, USA

Abstract

Users may view, print, copy, and download text and data-mine the content in such documents, for the purposes of academic research, subject always to the full Conditions of use: http://www.nature.com/authors/editorial_policies/license.html#terms

*Corresponding Authors: clabonne@northwestern.edu, tkw@msu.edu, ohallor8@msu.edu.

Author Contributions

J.F.S., A.S., N.J.Z., B.M.H., C.L., T.K.W., and T.V.O. designed the research. J.F.S., A.S., N.J.Z., R.B., and E.G.S. performed the research. B.L. helped design and implement XFM experiments and process and analyze the data. J.F.S., A.S., B.M.H., T.K.W., and T.V.O. wrote the manuscript. All the authors discussed the results and commented on the manuscript.

Competing Interests

The authors declare no competing financial interests.

Data Availability Statement

Data supporting the findings of this study are available within the article and its Supplementary Information files. The datasets generated during and analyzed during the current study are publicly available in the Figshare repository, at the following links: Confocal data for Figure 1, Supplemental Figure 1, and Videos 1 and 2: https://figshare.com/articles/dataset/Confocal_Images/14233235

XFM data for Figures 4 and 5 and Supplemental Figures 4, 5, and 6: https://figshare.com/articles/dataset/XFM_Data/14265332

AEM data for Figure 6 and Supplemental Figures 7, 8, and 9: https://figshare.com/articles/dataset/AEM_Data/14265350

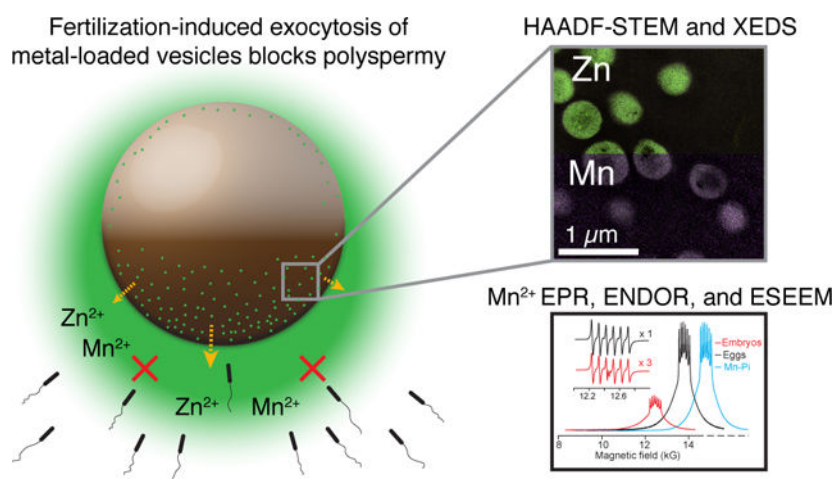
TEM cortical images for Supplemental Figure 10: https://figshare.com/articles/dataset/TEM_Cortical_Images/12827894/1

Animal Use Statement:

Animal procedures were approved by the Northwestern University Institutional Animal Care and Use Committee (NU-IACUC, animal assurance number D16-00182), under protocol IS00008873 (LaBonne), and are in accordance with the National Institutes of Health's Guide for the Care and Use of Laboratory Animals.

Mammalian oocytes undergo major changes in zinc content and localization in order to be fertilized, the most striking being the rapid exocytosis of over ten billion zinc ions, known as zinc sparks. Here we report that fertilization of amphibian *Xenopus laevis* eggs also initiates a zinc spark that progresses across the cell surface in coordination with dynamic calcium waves. This zinc exocytosis is accompanied by a newly recognized loss of intracellular manganese: synchrotron-based X-ray fluorescence and analytical electron microscopy reveal that zinc and manganese are sequestered in a system of cortical granules that are abundant at the animal pole. Through Electron-Nuclear Double-Resonance (ENDOR) studies, we rule out Mn^{2+} complexation with phosphate or nitrogenous ligands in intact eggs but the data are consistent with a carboxylate coordination environment. Our observations suggest that zinc and manganese fluxes are a conserved feature of fertilization in vertebrates and that they function as part of a physiological block to polyspermy.

Graphical abstract



Introduction

Physiochemical approaches are opening the door to understanding how inorganic chemistry regulates key biological processes. A striking example of this is the discovery of zinc regulatory pathways controlling fertilization of mammalian oocytes which begins with the coordinated uptake of billions of zinc ions in the brief final stages of meiotic maturation.¹ Upon fertilization, murine eggs then rapidly release between 10–20% of their zinc from a pool of 8,000 cortical vesicles in events described as zinc sparks.^{2,3} First observed using zinc responsive fluorescent probes in *M. musculus*², these events occur in macaques,² *B. taurus*⁴ and *H. sapiens*⁵ and are essential for transition of the egg into an embryo. Studies of mouse eggs reveal several roles of these zinc sparks: they regulate transitions from the meiotic to mitotic cell cycle of the egg and resulting zygote, and play roles in the slow block to polyspermy in the cell envelope.^{6,7} The magnitude of the zinc spark, readily established in real time using fluorescent probes, correlates with the quality of the resulting embryo.^{8,9} Analogous zinc-dependent phenotypes are observed in *Caenorhabditis elegans*¹⁰ and *Drosophila melanogaster*¹¹, where zinc availability is required for embryo viability.

While eggs from each of these provide specific advantages, each is limited by size and low material yields. This is not the case for the African Clawed Frog, *Xenopus laevis*.

While zinc is known to be transported into *Xenopus* oocytes over a period of months during oogenesis^{12,13} little is known about whether a zinc cycle occurs in this or other amphibians: neither influx nor exocytosis of zinc has been reported during meiosis. We decided to test whether meiotic zinc transients occur in *Xenopus* because of the large size and the abundance of eggs produced by the frog. The diameter of *Xenopus* eggs is fifteen times that of mouse eggs, allowing for a more in-depth study of the dynamics of the zinc efflux. While the abundance of auto-fluorescent yolk platelets in frog eggs presents challenges in confocal microscopy studies, the large size and the fact that a typical frog extrudes hundreds of eggs at a time, each with an average dry weight of 0.45 mg/egg,¹⁴ allows for the application of methods such as Inductively Coupled Plasma Mass Spectrometry (ICP-MS) and Electron-Paramagnetic Resonance (EPR) that otherwise would require an formidably large number of mammalian eggs. These bulk-sample methods provide key benchmarks and allow for our application of an array of more sensitive quantitative methods for understanding the chemistry of metal ion fluctuations in the regulation of biological processes at both the single cell and subcellular level.

Here, we present several complimentary physical methods that show that fertilization triggers release of zinc from vesicular storage compartments at the surface of the frog egg. These cortical vesicles, located predominantly at the animal pole, are the source. Our results suggest that the storage of labile zinc complexes and their triggered release as zinc sparks may be an evolutionarily conserved and functional feature of fertilization from amphibians to mammals. Intriguingly, *Xenopus* differs from mammals by also concentrating manganese in cortical vesicles and releasing a significant amount of the egg's Mn^{2+} content at the time of fertilization. We find that extracellular Zn^{2+} or Mn^{2+} decreases the rate of *Xenopus* fertilization, suggesting that the triggered release of these metal ions contributes to blocking the entry of a second sperm which would be fatal to a developing embryo. The paramagnetism of Mn^{2+} allows us to glean insights into the local coordination environment of manganese within the cortical granules in ways that are not possible for its d^{10} congener Zn^{2+} . These chemical and functional insights into the inorganic chemistry of an amphibian egg expand the evolutionary context of zinc, and possibly now manganese, fluctuations as signaling events in biology.

Results

The zinc spark is conserved in amphibia

Live cell fluorescent microscopy experiments using the fluorescent zinc-responsive probe FluoZin-3 were employed to test whether zinc is released from *Xenopus* eggs upon fertilization or activation by chemical treatment. Following the addition of sperm, a single zinc release event is observed. Moreover, beginning at a single point on the oocyte surface, zinc release proceeds bidirectionally around the circumference of the egg, taking around 3 minutes to reach the opposite point (Figure 1A, Video 1). The zinc spark in mammalian oocytes has been shown to be a calcium-dependent exocytosis event, and the Ca^{2+} ionophore ionomycin is known to parthenogenetically activate amphibian eggs.¹⁵

Using these conditions as a guide, the addition of 20 μM ionomycin to frog eggs leads to a single rapid and intense release of zinc (Figure 1B, Video 2). The zinc efflux induced by addition of ionomycin starts at a broad section of the circumference and travels around the circumference of the egg within approximately 30 – 90 seconds.

Upon fertilization, the zinc efflux travels approximately linearly around most of the circumference of the egg at $9.7 \pm 0.3 \mu\text{m}/\text{sec}$ ($n = 3$, mean \pm SD). Figure 1C and D show the rate of efflux around the circumference (see Supplemental Figure 1 for procedure). Fertilization is known to initiate a well-established biochemical cascade leading to calcium release from intracellular stores.¹⁶ This is apparent in the calcium wave, which travels at an average of $8.9 \mu\text{m}/\text{s}$ ¹⁷, similar to that of our observed zinc efflux. The calcium wave starts at the site of sperm entry, and travels around the egg in approximately 3.5 minutes¹⁷, about as long as the zinc spark, suggesting that the calcium wave triggers zinc release. Zinc release in eggs activated by ionomycin is more rapid, likely because ionomycin is bringing calcium indiscriminately to all parts of the egg simultaneously, leading to a faster release of cortical granule (CG) content. Zinc is known to be a cofactor for the ZPA protease, which is released from *Xenopus* eggs and hardens the ZPA glycoprotein following fertilization, contributing to the block to polyspermy.¹⁸ Given that the zinc-binding affinity of FluoZin-3 (K_D 9.1 nM)¹⁹ is lower than that of most known zinc proteins,^{3,20} the observed extracellular fluorescence signal is likely arising from free zinc.

The change in intracellular distribution of this cofactor resulting from zinc efflux can be mimicked by treatment with intracellular metal chelating agents. In mouse eggs, treatment with these agents leads to parthenogenic egg activation supporting the conclusion that zinc efflux is necessary for activation.² To test whether this is true in frog as well as in mammals, *Xenopus* eggs were treated with cell-permeable chelators and scored for activation. Treatment with N,N,N',N'-tetrakis-(2-pyridylmethyl)-ethylenediamine [TPEN] does not activate frog eggs, probably due to its low solubility; however, treatment with 1,10-phenanthroline (OP) activates $97 \pm 5\%$ of the eggs (Mean \pm SD, $n = 3$. See Supplemental Figure 2, Videos 3 – 5). To test whether OP causes activation through lowering intracellular copper availability, eggs were treated with ammonium tetrathiomolybdate (TTM), which has a high selectivity and specificity for copper.²¹ TTM did not activate the eggs (Video 6) indicating that activation is driven by a decrease in zinc, instead of a decrease in copper availability. The absence of validated intracellular chelators that are specific for other transition metals limits our ability to address their roles in the activation of mammalian or amphibian eggs.

Fertilization-induced changes in metal content

While the zinc content of mouse eggs drops circa 20% upon fertilization, a previous study using atomic absorption spectroscopy revealed no difference in the zinc content of single *Xenopus* eggs and embryos.¹³ To determine whether zinc content changes immediately following fertilization, we analyzed eggs and embryos using Inductively Coupled Plasma Mass Spectrometry (ICP-MS). We compared eggs to embryos collected one-hour post-fertilization and found no statistically significant change in zinc content (Figure 2A).

Fluorescence optical microscopy nonetheless clearly indicates that zinc is released upon fertilization; we hypothesize that this release corresponds to only a small percentage of the total zinc contained in these large eggs. In contrast to mammalian eggs, at the time of fertilization approximately 90% of intracellular zinc in *Xenopus* eggs is found in the yolk.^{12,22} As discussed in detail below, it is not surprising that only a very small proportion of intracellular zinc ions is released.

We also determined concentrations of other transition metals before and after fertilization. There was no change in the average iron or copper concentration following fertilization. However, intracellular manganese decreased by $53 \pm 15\%$ ($n = 4$, \pm SEM) (Figure 2A). We did not detect changes in other elements (Figure 2B and Supplemental Table 1 for values in atoms/cell). As this was an unexpected finding, we decided to probe it further.

The coordination environment of manganese

Intracellular manganese is predominantly present in the +2 oxidation state.^{23,24} The majority of that is found in kinetically labile complexes with low molecular-weight metabolites,^{25–28} but it is also bound as a cofactor in a number of enzymes.²⁹ Mn^{2+} is paramagnetic ($S=5/2$), and we employ a combination of Electron-Paramagnetic Resonance (EPR), Electron-Nuclear Double-Resonance (ENDOR) and Electron Spin-Echo Envelope Modulation (ESEEM) spectroscopies, complementary means of obtaining an NMR spectrum of the ligands to a paramagnetic metal ion (see Supplemental Methods), to determine the relative populations of the different Mn-ligand complexes present in intact eggs before and after fertilization.^{25,26,28}

The absorption-display continuous-wave (CW) EPR spectrum of frozen intact eggs and embryos provides a well resolved six-line pattern created by the hyperfine interaction of the electron spin with ^{55}Mn nuclear spin ($I = 5/2$). This pattern is centred around magnetic field of $\sim 12kG$, and rides on relatively narrow “wings” (Figure 3A and see SI); the latter are suppressed in derivative-mode CW EPR spectra (inset). This pattern is typical of Mn^{2+} coordinated in high-symmetry (roughly octahedral) geometry, as seen for small Mn-metabolite complexes like Mn-phosphate (Mn-Pi). Broad “wings” associated with asymmetric Mn^{2+} chelate and enzyme environments (i.e. MnSOD)^{27,28} are absent in the spectra of *Xenopus* eggs and embryos. The shape of the Mn^{2+} EPR spectrum of the embryos is unchanged from that of the eggs (Supplemental Figure 3) but the amplitude of the embryo signal is about one-third that of the eggs ($\sim 30 \pm 10\%$ remaining; see Figure 3, legend, and Supplemental Methods). Given that the spectra have the same shape, their relative amplitudes are an appropriate measure of Mn^{2+} present. The decrease in EPR amplitude upon fertilization agrees with the loss of Mn measured by ICP-MS (Figure 2), within the mutual uncertainties of the measurements, together showing that the egg loses Mn^{2+} upon fertilization.

ENDOR and ESEEM were used to determine the intracellular speciation of the Mn^{2+} . Figure 3B shows 35 GHz pulsed ENDOR spectra of eggs and embryos (triplicates) and selected exemplar Mn^{2+} complexes (hexa-aquo Mn^{2+} and the Pi, and polyphosphate [polyP]). The $[Mn-(H_2O)_6]^{2+}$ sample shows a strong 1H ENDOR response with multiple peaks centered at the 1H Larmor frequency (shown under the 1H ‘brace’) assigned to

directly-coordinated water molecules.³⁰ When a metabolite moiety such as a phosphate binds to Mn^{2+} it replaces coordinated water(s), decreasing the ^1H ENDOR amplitude. When a phosphate binds, this also introduces a ^{31}P ENDOR doublet, split by the electron-nuclear interaction and centered at the ^{31}P Larmor frequency (shown under the 'brace' ^{31}P). In Mn-polyP complexes, multiple phosphates bind, most of the waters are displaced, as shown by the large reduction of ^1H ENDOR signal, and there is an even greater increase in ^{31}P ENDOR signal (Figure 3B). When the amplitudes of the ^{31}P , ^1H ENDOR peaks shown in Figure 3B as gray stripes are normalized to the corresponding Mn^{2+} concentrations they are denoted as absolute ENDOR responses and labelled as $^{31}\text{P}\%$, $^1\text{H}\%$. These responses can be used in a heuristic model of Mn^{2+} ligand binding described previously²⁶ to estimate fractions of aquo, Pi, polyP, and ENDOR-silent (e.g. carboxylate) complexes (see SI).

In comparison to the exemplars, both eggs and embryos show weak ^{31}P signals (inset a), indicating little Pi/polyP ligation, and a weak $^1\text{H}\%$ ENDOR response (inset b), yet indicating a high population of ligands that displace H_2O . To test for Mn^{2+} ligation by nitrogenous ligands we used 35 GHz ESEEM spectroscopy, which is a very sensitive probe towards such ligation^{25–28}; Figure 3C shows that the ESEEM time-wave for a frozen solution of Mn^{2+} -imidazole exhibits strong modulation whose frequency corresponds to ^{14}N resonance frequencies. Neither eggs nor embryos show any ^{14}N modulation of the time-waves in the 35 GHz ESEEM traces, indicating the absence of any detectable Mn-N complexes. Together, these observations indicate that the majority of the intracellular Mn^{2+} coordination sites (i.e. between 75–90%) in both eggs and embryos are occupied by ENDOR (NMR)-silent ligands, and when an organism is grown with natural abundance ^{12}C nutrients, carboxylates are the major class of such ligands. We conclude that the majority Mn^{2+} population in the eggs and embryos can be assigned as low molecular-weight Mn^{2+} complexes with carboxylate ligands (Mn-C 75–90%).

Disruption of eggs exposes compartmentalized Mn^{2+} complexes to cytoplasmic concentrations of phosphate and phosphoryl ligands which are typically in the millimolar concentration range.³¹ As a result, scrambling induces a 20% increase in the Mn-P population (Supplemental Figure 3 and Supplemental Methods). Taken together, the ENDOR measurements are consistent with a model in which a majority of the EPR-detectable Mn^{2+} is sequestered as manganese-carboxylate in non-cytosolic compartments in the egg, and that these complexes are released from the egg upon fertilization without change in speciation of the remaining Mn^{2+} . To test for the presence of Mn- and Zn-enriched compartments in these eggs we turned to two subcellular methods for mapping the locations of elements in cells.

XFM reveals cortical metal compartmentalization

X-ray Fluorescence Microscopy (XFM)³² methods indicated that cortical vesicles in mouse eggs contain on average one million zinc ions each³ and we employed this approach to test for the presence of analogous zinc- and manganese-enriched sites in small sections at the cortices of *Xenopus* eggs and embryos. To preserve transition metal contents in our samples we used a modified form of Timm's silver staining.^{3,33,34} ICP-MS reveals that this fixation method preserves native metal contents in *Xenopus* eggs, except for iron, which showed

a significant gain in concentration, due to contamination in the fixative (Seeler et al., in preparation). We analyzed ultramicrotome slices of the animal pole (AP) and vegetal pole (VP) of eggs and embryos, ranging from 0.4 to 2 μm thick. The cortical ultrastructure of the AP and VP are greatly different.³⁵ We find that metal content and localization differ in the poles as well (Figure 4 and Supplemental Figures 4 and 5). We conclude that in *Xenopus* eggs, zinc is loaded to high concentrations in the smaller group of cortical vesicles that are analogous to those found in murine, bovine and primate eggs.^{2,4,5}

We find two classes of metal-containing compartments: the smaller ones are far more abundant in the AP than the VP. Fitting the XFM data reveals that metals are localized in compartments at millimolar-scale concentrations. Figure 5A presents the XFM values as $\mu\text{g}/\text{cm}^2$ next to an estimate of the minimal molar concentration in each site. The conversion to mM was obtained through estimates of the number of atoms in each voxel, as the sample thickness is known (see SI for more detail). There is some variation in the metal content of these compartments, though some of this is because slices of eggs were analyzed, so compartments may represent sections or combinations of what we assume to be vesicles (Figure 5B and C). There is metal concentration in these compartments: Mn concentration is approximately 30X higher in the compartments compared to the entire volume of the egg (see Figure 2B), Cu is 150X, and Zn is 10X.

The second class of metal-containing compartments is larger and contains a lower concentration of metal. These are likely yolk platelets. Yolk consists of two proteins: lipovitellin, which binds zinc, and phosvitin, which contains 25% phosphoserine.³⁶ These compartments are also larger in the VP cortex than the AP,³⁷ further supporting this assignment. Besides zinc and to an extent copper, transition metals are at very low concentrations in the yolk platelets (Supplemental Table 2).

Unlike mammalian eggs, we find other metals in addition to zinc localized to the *Xenopus* egg cortex. To determine the extent of metal co-localization, Pearson coefficients were calculated. The egg AP sections had the greatest amount of correlation with low variability (Supplemental Figure 6). Two main elemental groupings with high Pearson coefficients (0.64 – 0.92) are observed. The first is cobalt, copper, and nickel, and the second is calcium, manganese and zinc. A possible source of metals with little or no known biological role in vertebrates (e.g. cobalt and nickel) is the water in which the animals are housed. Water from frog tanks was analyzed by ICP-MS and transition metals were found to be at approximately nanomolar concentrations (Supplemental Table 3).

While XFM provides very high elemental sensitivity, the spatial resolution at 2-ID-D (300 \times 300 nm pixels) does not allow for high resolution imaging of the metal-enriched sites. Thus, additional high-resolution elemental mapping methods were employed to characterize these sites.

AEM demonstrates metal vesicular localization

To assess whether these sites represented metal-enriched vesicle structures, nanometer resolution images were obtained using state-of-the-art Analytical Electron Microscopy (AEM) which combines Scanning Transmission Electron Microscopy (STEM) with X-ray

Energy Dispersive Spectroscopy (XEDS).³⁸ Images were obtained using 150 nm-thick sections of eggs and embryos. Similar to the XFM data, AEM revealed two classes of vesicle, with the smaller ones containing multiple metals, and the larger ones containing primarily phosphorous and sulfur, with very low concentrations of the other elements examined (Figure 6A and B). Ca, Mn, Co, Ni, Cu, and Zn are found in the smaller class of electron-dense vesicle (Figure 6C). The average diameter of the small vesicle in the egg AP is 490 ± 56 nm (mean \pm SD, $n = 50$) (Figure 6D). These images concur with our XFM findings. There are fewer small vesicles in the animal pole embryo than in the egg (Supplemental Figure 7). Both the vegetal pole egg (Supplemental Figure 8) and vegetal pole embryo (Supplemental Figure 9) show large yolk platelets and few of the small vesicles.

Using TEM images of sections of the circumferences of an egg and embryo AP, we counted the numbers of small, electron-dense vesicles in the cortex. Within $10 \mu\text{m}$ of the plasma membrane, there was an average of 21 vesicles/ $100 \mu\text{m}^2$ in the egg, compared to an average of 3.4 vesicles/ $100 \mu\text{m}^2$ in the embryo, corresponding to an 84% drop (Supplemental Figure 10). We can therefore conclude that we see an almost complete release of cortical vesicle content. Additionally, this analysis suggests that other vesicular metals beside zinc and manganese are released from the zygote following fertilization. Finally, we sought to determine the biological relevance of this metal release.

Treatment with Zn or Mn decreases the fertilization rate

To determine if the zinc and/or manganese released from *Xenopus* eggs following fertilization prevents polyspermy, we fertilized eggs in buffer containing different concentrations of the two metals. Increasing concentrations of both zinc and manganese (Figure 7, Supplemental Table 4; see Supplemental Figures 11 and 12 for raw data) lead to decreasing rates of fertilization. This was determined by the percent of eggs that become properly-cleaving embryos (after normalization to a control fertilization), divided by the total count of eggs, embryos, and failed cleavage (Figure 7A). Zinc inhibits fertilization at an order of magnitude lower concentration than that of manganese: a 50% block to fertilization occurs at $53 \mu\text{M}$ (95% CI = $47 - 61 \mu\text{M}$) in ZnSO_4 treatments (Figure 7B), while it occurs at $890 \mu\text{M}$ (95% CI = $770 \mu\text{M} - 1.0 \text{mM}$) in the case of MnCl_2 (Figure 7C).

Discussion

The goal of this study was to determine whether zinc is aggregated in a system of vesicles near the surface of *Xenopus* eggs and then released in a highly coordinated manner, similar to what has been shown for mammalian model organisms and human eggs. Indeed, we show that *Xenopus* eggs, like mammalian ones, undergo zinc-chelator induced activation, contain a similar system of zinc-loaded vesicles, albeit larger than those seen in mammalian eggs,³ as well as demonstrate an efflux of zinc following activation and fertilization. Thus, these reorganizations of zinc are essential to successful development in mouse and *Xenopus*. We demonstrate that one function of the zinc released acts as part of a block to fertilization in *Xenopus*: the entry of a second sperm is typically catastrophic in early embryonic development. Further experiments are necessary to determine if, as in mouse eggs, zinc

alters the structure of the outer envelope in *Xenopus* eggs. It is possible that release into the jelly coat could have an effect as well.

Surprisingly, we find that manganese is released alongside zinc in *Xenopus* eggs. Manganese, as well as a series of non-essential transition metal ions, is stored in vesicular compartments. Several lines of reasoning support the conclusion that the cohort of small metal-containing vesicles describe here are CGs. First, the timing of the zinc spark in *Xenopus* eggs correlates directly to the well-established process of CG breakdown. CG breakdown begins around 3 minutes post-fertilization (approximately the time needed for the sperm to penetrate the egg) and virtually all CGs have ruptured within 10 minutes.^{35,39} Second, the spatial distribution of CGs resembles that of the metal-containing compartments. CGs in the AP are mostly next to the plasma membrane, while those in the VP can be located farther into the cortex.³⁵ Third, the reported sizes of CGs – 1.5 – 2.5 μm ^{35,40} – are similar to those of the metal-containing compartments. Although the vesicles described here appear smaller than the literature values, this is likely an effect of fixation and/or treatment with sodium sulfide. The zinc-containing CGs of mouse eggs are approximately 260 nm in diameter and have an intra-vesicular zinc content of 0.2 M.³ *Xenopus* CGs are therefore larger but have lower zinc concentrations.

The role of cobalt and nickel loading in *Xenopus* CGs is currently unknown. Because of their toxicity, these metals may be sequestered in the egg CGs to minimize teratogenicity. It is also possible that the metals are not intentionally localized to CGs, but rather are mistaken for Zn^{2+} and Mn^{2+} by promiscuous divalent metal transporters. Sequestration and release of these metals may be specific to amphibians; we will further explore this in mouse.

These results in *Xenopus* provide evidence of the Mn^{2+} coordination environment in an egg. While the EPR and ENDOR signals drop as expected upon fertilization, the speciation of Mn remaining after Mn release at fertilization remains largely unchanged. Most importantly, both eggs and embryos have only a minimal population of Mn-Pi and polyP complexes (~10%), with most Mn carboxylate-bound (75–90%), and with negligible amounts bound in high molecular weight proteins/enzymes such as MnSOD. The coordinating carboxylates are presumed to be associated with low molecular weight metabolites. This type of insight into the manganese coordination environment in small subcellular compartments provides a starting point for understanding the chemistry of other metal ions in these highly specialized compartments.

Manganese content of eggs was not directly determined in our studies of mouse, worm, and cow as yields of eggs in these systems are too low to analyze with ICP-MS. Previously published single cell data on mouse eggs was acquired on XFM beamlines that did not provide sufficient incident flux for detection of manganese signals; however the single cell studies described here open the door to the evaluation of these questions. While the role of the manganese efflux is not known, one possible role may be as a block to polyspermy. In a mouse model, Mn^{2+} inhibited sperm-zona pellucida interactions, with 50% inhibition at 1.25 mM MnCl_2 .⁴¹ This is similar to what we found in our *Xenopus* model, in which half of fertilization was inhibited at 890 μM MnCl_2 . Estimating the concentration of Mn released in the area around the *Xenopus* zygotes gives a value in the hundreds of micromolar range (see

SI for calculations). Thus our results are consistent with a model in which the Mn and Zn release functions in part to block the entry of a second sperm, though additional tests of this mechanism are required.

In conclusion, we have found that a zinc exocytosis event upon fertilization is evolutionarily conserved between mammals and amphibians. Additionally, we have found that manganese is also released from *Xenopus* eggs and that both metals can inhibit fertilization.

Methods

Additional details including descriptions of methods and calculations are included in Supplemental Information.

Confocal Imaging.

Xenopus eggs were obtained via established methods. Eggs were acquired from female *Xenopus laevis* (Nasco) between the ages of 3 to 10 years old. Confocal images were taken at 2.5X using a Leica SP5 microscope (Biological Imaging Facility, Northwestern University). Eggs were imaged in 0.1X Ca²⁺, Mg²⁺, and EDTA-free Marc's Modified Ringer's (MMR: 10 mM NaCl, 200 μM KCl, 500 μM HEPES pH 7.4) buffer containing 50 μM FluoZin-3 tetrapotassium salt (ThermoFisher Scientific) and implement XFM experiments and process and analyze) In order to parthenogenically activate the eggs, ionomycin calcium salt from *Streptomyces globatus* (Sigma Aldrich) in DMSO was added to the buffer at a final concentration of 20 μM. To image fertilization, around half of a testis was ground in 200 μl 1X Ca²⁺, Mg²⁺, and EDTA-free MMR (100 mM NaCl, 2 mM KCl, 5 mM HEPES pH 7.4) and kept on ice. Before imaging, the sperm solution was mixed 1:1 with 0.1X Ca²⁺, Mg²⁺, and EDTA-free MMR and added at a 1:10 dilution to the buffer in the imaging dish.

ICP-MS.

The jelly coat of eggs and embryos was removed through soaking in a 3% w/v solution of cysteine-HCl, pH 8 for 10 minutes. They were rinsed and then 20 egg/embryos were placed in a metal-free conical tube. 3–5 tubes of eggs/embryos were analyzed for each of the 4 separate frogs. The eggs/embryos were dried in a heat block and dissolved in 450 μl 67–70% trace-metal free nitric acid (Supelco) overnight at 70 C. The solution was diluted to 15 ml using MilliQ H₂O. Metal concentrations were measured using a Thermo iCAP Q ICP-MS and a Thermo iCAP 7600 ICP-OES (Quantitative Bio-element Imaging Center, Northwestern University). The elemental composition of frog tank water was measured using a Thermo iCAP Q ICP-MS and a Thermo Element2 High Resolution Magnetic Sector Field ICP-MS (Quantitative Bio-element Imaging Center, Northwestern University)

EPR/ENDOR/ESEEM Spectroscopy.

Frog eggs and embryos were loaded into a quartz EPR sample tube, flash-frozen in liquid nitrogen, and stored at 77 K until analysis. 35 GHz continuous-wave (CW) EPR spectra were recorded using a lab-built 35 GHz EPR spectrometer.⁴² Absorption-display EPR spectra were collected from eggs/embryos and Mn-metabolites by using CW “rapid

passage” methods at 2 K as previously described.^{25,27} Pulsed ENDOR/ESEEM spectra were recorded using a lab-built 35 GHz pulsed EPR spectrometer.⁴³ All spectra were recorded at 2 K using an immersion helium cryostat. Experiments were performed on three sets of samples and the average ³¹P%, ¹H% were used to calculate the fractional Mn²⁺ speciation. The fractional populations of Mn-L, L = H₂O, Pi, polyP, and ENDOR-silent complexes reported as percentages were obtained using a heuristic binding model as previously described.²⁶

Sample Fixation and XFM.

Eggs/embryos were fixed in a solution containing NaSH (2.5% glutaraldehyde, 2% paraformaldehyde, 20 mM NaSH, in 0.1 M PIPES buffer, pH 7.4) for 2 hours at RT. They were then dehydrated in EtOH. After dehydration, eggs/embryos were infiltrated with a Durcupan resin and polymerized at 65° C for 24 hours. Sections of 400 nm and 2 μm thickness were obtained with a Ultracut-S ultramicrotome (Leica) using a diamond knife (Diatome/EMS). Egg and embryo sections were mounted on 200 nm-thick silicon nitride windows (Norcada) and were glued to aluminum sample holders using clear nail polish. The sections were imaged at Beamline 2-ID-D at the Advanced Photon Source at Argonne National Laboratory.

Analytical Electron Microscopy.

Eggs and embryos used in AEM studies were fixed as above. ~ 150 nm thick ultramicrotome-cut sections were mounted on an aluminum grid coated with a Formvar and a carbon film and mounted in a custom-manufactured beryllium-tipped cryo-transfer tomography holder from Fischione Instruments. Experimental measurements were performed using a ThermoFisher Talos F20 and the prototype ANL PicoProbe AEM's, both equipped with the most recent generations of high solid angle (~ 1sr) X-ray energy dispersive spectroscopy systems. All observations were made at 200 kV in both TEM and STEM modes at room temperature. Temporally resolved hyper spectral imaging (HSI) was used to scan variable area regions of interest at spatial resolutions ranging from 2–100 nm. Probe currents employed were typically ~ 100 pA, HSI regions of interest utilized pixel dwell times of ~ 25 μsec/pixel for hundreds of frames to develop statistics and mitigate drift, resulting in final data acquisition times of ~ 500 msec/pixel. Programs used for data acquisition and analysis were ThermoFisher Scientific TIA/ESVision and ThermoFisher Scientific Velox.

Fertilization Experiments.

Eggs were placed in 0.1X EDTA-free MMR containing different concentrations of ZnSO₄ or MnCl₂ for 15 minutes. They were fertilized using a sperm solution containing the same metal concentration. 15 minutes after fertilization, the dishes were flooded with the corresponding metal solutions. After cleavage became apparent, eggs were scored between uncleaved, properly cleaved, and failed cleavage. The percent of eggs properly cleaved in the experimental groups was normalized to that of a control group fertilized in buffer that was not spiked with zinc or manganese.

Supplementary Material

Refer to Web version on PubMed Central for supplementary material.

Acknowledgments

Note added in proof: A recent report by Wozniak, K. L. et al. published while this paper was in revision corroborates the idea that zinc sparks can contribute to blocking polyspermy in *Xenopus* (PLoS Biol. 18, 2020).

This research is supported by NIH grants R01GM115848 to TVO and TKW, R01GM038784 and P41GM181350 to TVO, and R01GM111097 to BMH. JFS was supported by The Cellular and Molecular Basis of Disease Training Program at Northwestern University (NIH T32GM008061), NJZ was supported by both LDRD funding No. 2017-153-N0 and the Photon Science Division at Argonne National Laboratory. X-ray fluorescence microscopy was performed at the Advanced Photon Source (APS), while Analytical Electron Microscopy was performed using the ANL PicoProbe as well as AEM resources in the Center for Nanoscale Materials (CNM), both of which are Office of Science user facilities at Argonne National Laboratory. Use of the APS and CNM was supported by the U.S. Department of Energy, Office of Science, Office of Basic Energy Sciences, under Contract No. DE-AC02-06CH11357. This work made use of the BioCryo facility of Northwestern University's NUANCE Center, which has received support from the Soft and Hybrid Nanotechnology Experimental (SHyNE) Resource (NSF ECCS-1542205); the MRSEC program (NSF DMR-1720139) at the Materials Research Center; the International Institute for Nanotechnology (IIN); and the State of Illinois. Microscopy was performed at the Biological Imaging Facility at Northwestern University (RRID: SCR_017767), supported by the Chemistry for Life Processes Institute, the NU Office for Research, and the Department of Molecular Biosciences. Elemental analysis was performed at the Northwestern University Quantitative Bio-element Imaging Center supported by the Office of the Director, National Institutes of Health via NIH grants S10OD026786 and S10OD020118. We thank Ryan Woodruff and Lukas Gross for the initial discovery of zinc fluxes in frog eggs, Dr. Jessica Hornick and Dr. Seth Garwin for assistance with imaging, Dr. Keith MacRenaris, Omar Ali, and Rebecca Sponenburg for assistance with ICP-MS, and Dr. Paul Huber for assistance with *Xenopus* experiments.

References

1. Kim AM, Vogt S, O'Halloran TV & Woodruff TK. Zinc availability regulates exit from meiosis in maturing mammalian oocytes. *Nat. Chem. Biol.* 6, 674–681 (2010). [PubMed: 20693991]
2. Kim AM et al. Zinc sparks are triggered by fertilization and facilitate cell cycle resumption in mammalian eggs. *ACS Chem. Biol.* 6, 716–723 (2011). [PubMed: 21526836]
3. Que EL et al. Quantitative mapping of zinc fluxes in the mammalian egg reveals the origin of fertilization-induced zinc sparks. *Nat. Chem.* 7, 130–139 (2015). [PubMed: 25615666]
4. Que EL et al. Bovine eggs release zinc in response to parthenogenetic and sperm-induced egg activation. *Theriogenology* 127, 41–48 (2019). [PubMed: 30639695]
5. Duncan FE et al. The zinc spark is an inorganic signature of human egg activation. *Sci. Rep.* 6, 24737 (2016). [PubMed: 27113677]
6. Kong BY et al. Maternally-derived zinc transporters ZIP6 and ZIP10 drive the mammalian oocyte-to-egg transition. *Mol. Hum. Reprod.* 20, 1077–1089 (2014). [PubMed: 25143461]
7. Que EL et al. Zinc sparks induce physiochemical changes in the egg zona pellucida that prevent polyspermy. *Integr. Biol. (Camb.)* 9, 135–144 (2017). [PubMed: 28102396]
8. Kong BY et al. The inorganic anatomy of the mammalian preimplantation embryo and the requirement of zinc during the first mitotic divisions. *Dev. Dyn.* 244, 935–947 (2015). [PubMed: 25903945]
9. Zhang N, Duncan FE, Que EL, O'Halloran TV & Woodruff TK. The fertilization-induced zinc spark is a novel biomarker of mouse embryo quality and early development. *Sci. Rep.* 6, 22772 (2016). [PubMed: 26987302]
10. Mendoza AD, Woodruff TK, Wignall SM & O'Halloran TV. Zinc availability during germline development impacts embryo viability in *Caenorhabditis elegans*. *Comp. Biochem. Physiol. C Toxicol. Pharmacol.* 191, 194–202 (2017). [PubMed: 27664515]
11. Hu Q et al. Zinc Dynamics during *Drosophila* Oocyte Maturation and Egg Activation. *iScience* 23, 101275 (2020).

12. Falchuk KH, Montorzi M & Vallee BL. Zinc uptake and distribution in *Xenopus laevis* oocytes and embryos. *Biochemistry* 34, 16524–16531 (1995). [PubMed: 8845382]
13. Nomizu T, Falchuk KH & Vallee BL. Zinc, iron, and copper contents of *Xenopus laevis* oocytes and embryos. *Mol. Reprod. Dev.* 36, 419–423 (1993). [PubMed: 8305203]
14. de Laat SW, Buwalda RJ & Habets AM. Intracellular ionic distribution, cell membrane permeability and membrane potential of the *Xenopus* egg during first cleavage. *Exp. Cell Res.* 89, 1–14 (1974). [PubMed: 4435056]
15. Snow P, Yim DL, Leibow JD, Saini S & Nuccitelli R. Fertilization stimulates an increase in inositol trisphosphate and inositol lipid levels in *Xenopus* eggs. *Dev. Biol.* 180, 108–118 (1996). [PubMed: 8948578]
16. Stith BJ. Phospholipase C and D regulation of Src, calcium release and membrane fusion during *Xenopus laevis* development. *Dev. Biol.* 401, 188–205 (2015). [PubMed: 25748412]
17. Fontanilla RA & Nuccitelli R. Characterization of the sperm-induced calcium wave in *Xenopus* eggs using confocal microscopy. *Biophys. J.* 75, 2079–2087 (1998). [PubMed: 9746550]
18. Lindsay LL & Hedrick JL. Proteolysis of *Xenopus laevis* egg envelope ZPA triggers envelope hardening. *Biochem. Biophys. Res. Commun.* 324, 648–654 (2004). [PubMed: 15474476]
19. Marszalek I et al. Revised stability constant, spectroscopic properties and binding mode of Zn(II) to FluoZin-3, the most common zinc probe in life sciences. *J. Inorg. Biochem.* 161, 107–114 (2016). [PubMed: 27216451]
20. Fahrni CJ & O'Halloran TV. Aqueous Coordination Chemistry of Quinoline-Based Fluorescence Probes for the Biological Chemistry of Zinc. *J. Am. Chem. Soc.* 121, 11448–11458 (1999).
21. Smirnova J et al. Copper(I)-binding properties of de-coppering drugs for the treatment of Wilson disease. α -Lipoic acid as a potential anti-copper agent. *Sci. Rep.* 8, 1463 (2018). [PubMed: 29362485]
22. Auld DS, Falchuk KH, Zhang K, Montorzi M & Vallee BL. X-ray absorption fine structure as a monitor of zinc coordination sites during oogenesis of *Xenopus laevis*. *Proc. Natl. Acad. Sci. U. S. A.* 93, 3227–3231 (1996). [PubMed: 8622918]
23. Gunter TE et al. Determination of the oxidation states of manganese in brain, liver, and heart mitochondria. *J. Neurochem.* 88, 266–280 (2004). [PubMed: 14690515]
24. Ducic T et al. X-ray fluorescence analysis of iron and manganese distribution in primary dopaminergic neurons. *J. Neurochem.* 124, 250–261 (2013). [PubMed: 23106162]
25. Tsednee M et al. Manganese co-localizes with calcium and phosphorus in *Chlamydomonas* acidocalcisomes and is mobilized in manganese-deficient conditions. *J. Biol. Chem.* 294, 17626–17641 (2019). [PubMed: 31527081]
26. McNaughton R et al. Probing in vivo Mn²⁺ speciation and oxidative stress resistance in yeast cells with electron-nuclear double resonance spectroscopy. *Proc. Natl. Acad. Sci. U. S. A.* 107, 15335–15339 (2010). [PubMed: 20702768]
27. Sharma A et al. Across the tree of life, radiation resistance is governed by antioxidant Mn(2+), gauged by paramagnetic resonance. *Proc. Natl. Acad. Sci. U. S. A.* 114, E9253–e9260 (2017). [PubMed: 29042516]
28. Sharma A et al. Responses of Mn²⁺ speciation in *Deinococcus radiodurans* and *Escherichia coli* to gamma-radiation by advanced paramagnetic resonance methods. *Proc. Natl. Acad. Sci. U. S. A.* 110, 5945–5950 (2013). [PubMed: 23536297]
29. Horning KJ, Caito SW, Tipps KG, Bowman AB & Aschner M. Manganese Is Essential for Neuronal Health. *Annu. Rev. Nutr.* 35, 71–108 (2015). [PubMed: 25974698]
30. Tan X, Bernardo M, Thomann H & Scholes CP. Pulsed and continuous wave electron nuclear double resonance patterns of aquo protons coordinated in frozen solution to high spin MN²⁺. *The Journal of Chemical Physics* 98, 5147–5157 (1993).
31. Dworkin MB & Dworkin-Rastl E. Carbon metabolism in early amphibian embryos. *Trends Biochem. Sci.* 16, 229–234 (1991). [PubMed: 1891803]
32. Chen S et al. Synchrotron-based X-ray Fluorescence Microscopy as a Complementary Tool to Light Microscopy/Electron Microscopy for Multi-scale and Multi-modality Analysis. *Microsc. Microanal.* 24, 86–87 (2018).

33. Timm F. Zur Histochemie der Schwermetalle Das Sulfid-Silberverfahren. *Dtsch. Z. Gesamte Gerichtl. Med.* 46, 706–711 (1958). [PubMed: 13597613]
34. Danscher G, Stoltenberg M, Bruhn M, Søndergaard C & Jensen D. Immersion Autometallography: Histochemical In Situ Capturing of Zinc Ions in Catalytic Zinc-Sulfur Nanocrystals. *J. Histochem. Cytochem.* 52, 1619–1625 (2004). [PubMed: 15557216]
35. Grey RD, Wolf DP & Hedrick JL. Formation and structure of the fertilization envelope in *Xenopus laevis*. *Dev. Biol.* 36, 44–61 (1974). [PubMed: 4822839]
36. Montorzi M, Falchuk KH & Vallee BL. Vitellogenin and lipovitellin: zinc proteins of *Xenopus laevis* oocytes. *Biochemistry* 34, 10851–10858 (1995). [PubMed: 7662665]
37. Imoh H. Establishment and movement of egg regions revealed by the size class of yolk platelets in *Xenopus laevis*. *Roux Arch Dev Biol* 205, 128–137 (1995). [PubMed: 28306074]
38. Zaluzec NJ. Thin film characterization using analytical electron microscopy. *Thin Solid Films* 72, 177–192 (1980).
39. Kotani M, Ikenishi K & Tanabe K. Cortical granules remaining after fertilization in *Xenopus laevis*. *Dev. Biol.* 30, 228–232 (1973). [PubMed: 4735367]
40. Campanella C & Andreuccetti P. Ultrastructural observations on cortical endoplasmic reticulum and on residual cortical granules in the egg of *Xenopus laevis*. *Dev. Biol.* 56, 1–10 (1977). [PubMed: 838127]
41. Benau DA, McGuire EJ & Storey BT. Further characterization of the mouse sperm surface zona-binding site with galactosyltransferase activity. *Mol. Reprod. Dev.* 25, 393–399 (1990). [PubMed: 2109619]
42. Werst MM, Davoust CE & Hoffman BM. Ligand spin densities in blue copper proteins by q-band proton and nitrogen-14 ENDOR spectroscopy. *J. Am. Chem. Soc.* 113, 1533–1538 (1991).
43. Davoust CE, Doan PE & Hoffman BM. Q-Band Pulsed Electron Spin-Echo Spectrometer and Its Application to ENDOR and ESEEM. *Journal of Magnetic Resonance, Series A* 119, 38–44 (1996).

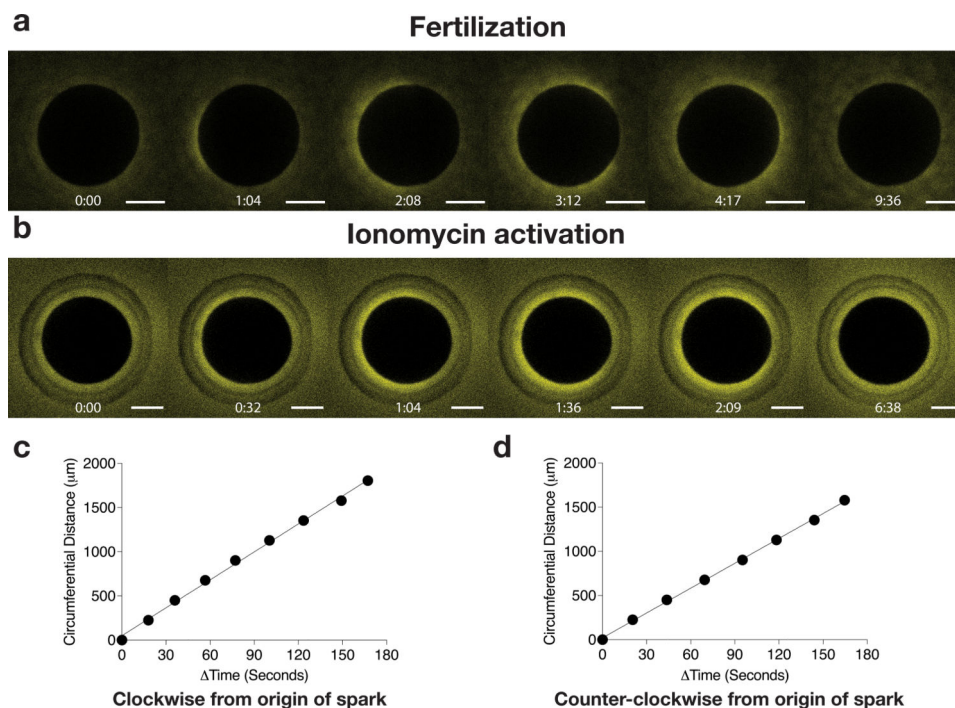


Figure 1: Zinc release from frog oocytes.

Zinc is released following both fertilization and chemical activation of a *Xenopus* egg.

a. Zinc efflux following fertilization of a *Xenopus* egg. Images are representative of 14 eggs from 4 separate frogs over 4 independent experiments. **b.** Zinc efflux following parthenogenic activation of a *Xenopus* egg by ionomycin. Images are representative of 12 eggs from 3 separate frogs over 3 independent experiments. In both **a.** and **b.** scale bar = 500 μm, time is as m:ss, and brightness and contrast have been adjusted for clarity (see Supplemental Methods for values). **c.** Representative plot of the circumferential distance from the origin of the zinc spark at which half-maximal fluorescence is measured over the time since the start of the spark, traveling clockwise from origin. **d.** Representative plot of the circumferential distance from the origin of the zinc spark at which half-maximal fluorescence is measured over the time since the start of the spark, traveling counterclockwise from origin. **c.** and **d.** are representative of measurements from 3 separate eggs (see text for mean rate).

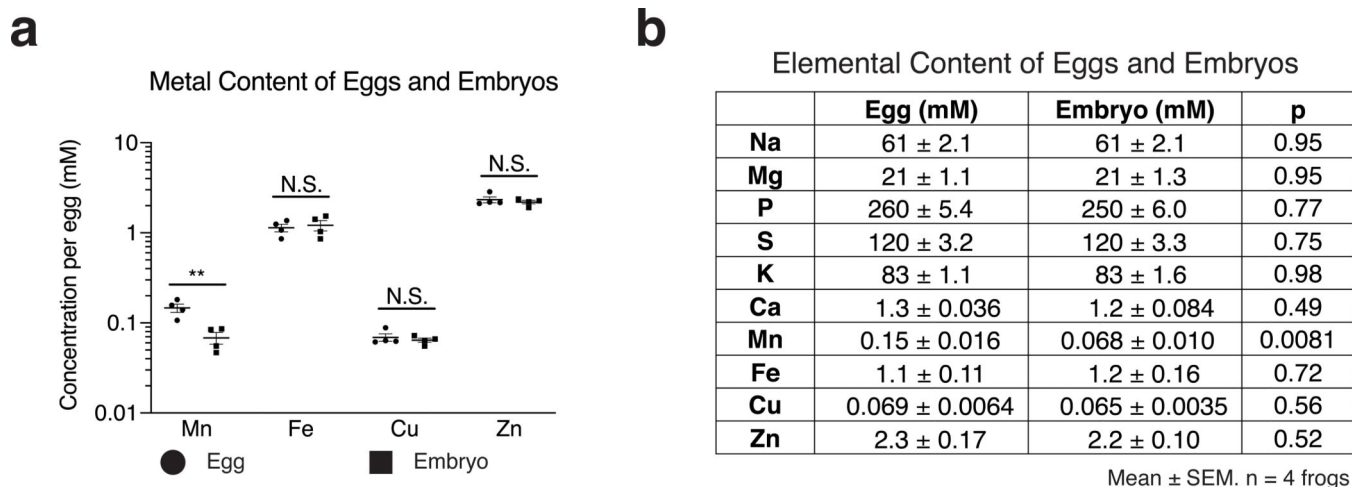


Figure 2: Elemental analysis of eggs and embryos.

ICP-MS measures a significant decrease in intracellular manganese post-fertilization. **a.** Metal concentrations of *Xenopus* eggs and embryos (1 hour post-fertilization) determined by ICP-MS. Intracellular Co and Ni are both below 13 μ M. Data are presented as mean \pm SEM per egg/embryo, **: $p = 0.0081$. Each point corresponds to ICP-MS analysis of a batch of 20 eggs normalized to a per egg basis. Similar results were obtained in 6 separate experiments (not shown). **b.** Elemental contents (mM) of *Xenopus* eggs and embryos (1-hour post-fertilization). Experimental conditions as in **a.** In both **a.** and **b.** n = samples from 4 separate frogs analyzed in a single ICP experiment. **p** is the significance of the change in elemental content following fertilization. Two-tailed, heteroscedastic T-tests were run between eggs and embryos in order to determine if there was a significant difference in metal content. No adjustments were made for multiple comparisons.

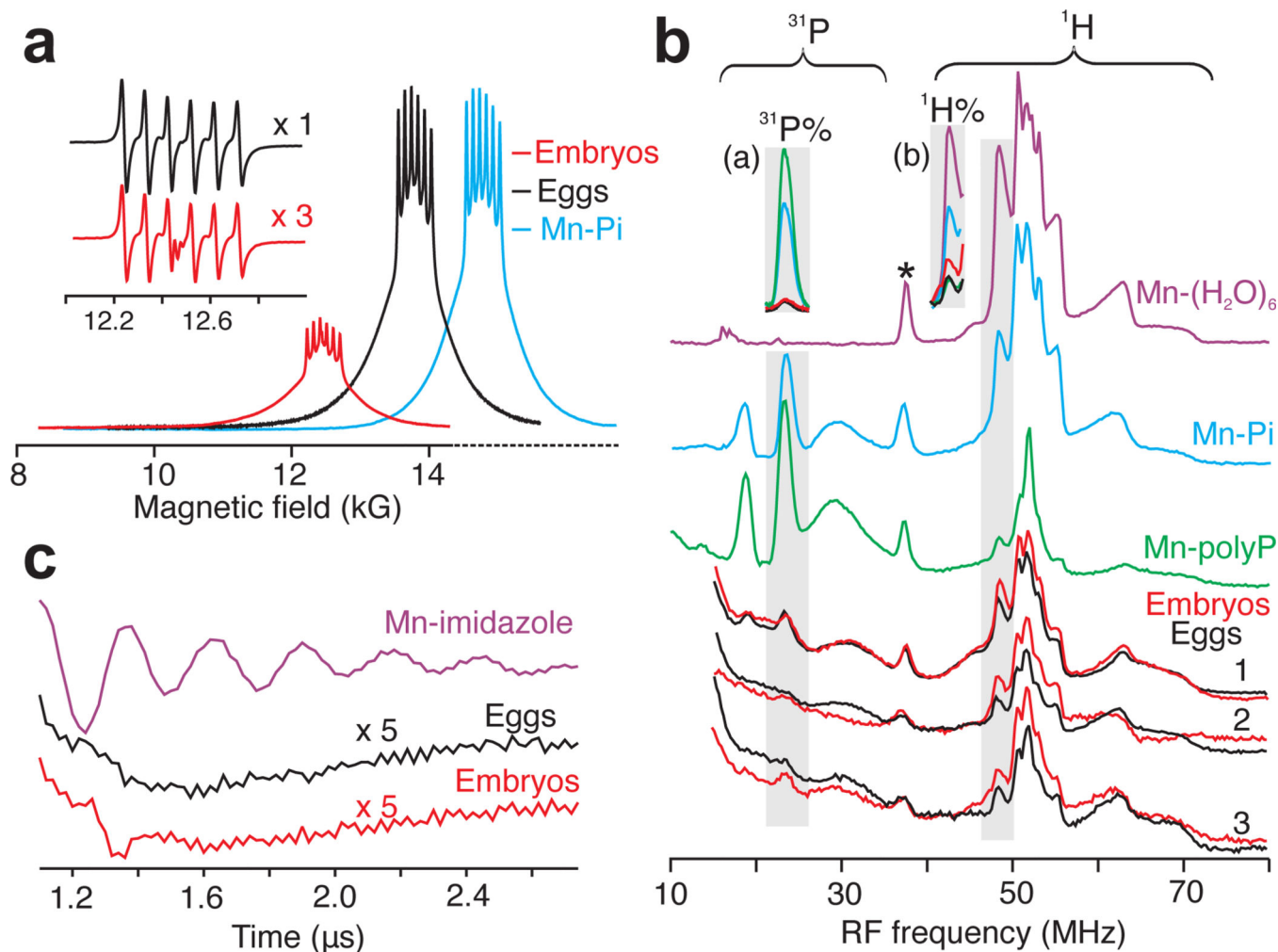


Figure 3: Paramagnetic resonance measurements of eggs and embryos.

EPR confirms a post-fertilization decrease in manganese, while EPR, ENDOR, and ESEEM demonstrate that the majority of intracellular manganese is bound to a low molecular weight carboxylate. 35-GHz, 2K EPR/ENDOR/ESEEM Spectra: **a**. Representative absorption-display CW-EPR spectra of Mn^{2+} in: frog eggs (black); embryos (red; 1/3 amplitude of eggs, $\sim 30 \pm 10\%$ remaining, see text); Mn-orthophosphates Mn-Pi (blue; scaled to eggs); EPR spectra of frog eggs/Mn-Pi offset by +1,350/+2,350. *Inset*: digital derivatives of the spectra, accentuating the six-line ^{55}Mn hyperfine pattern around 12kG magnetic field. **b**. $^{31}\text{P}/^1\text{H}$ Davies pulsed-ENDOR spectra of: intact frog eggs and embryos; solution Mn^{2+} complexes (aquo [H_2O], orthophosphate [Pi], polyphosphate [polyP]). Braces represent frequency ranges of ^{31}P and ^1H ENDOR signals. ENDOR spectra are normalized to Mn^{2+} concentration; thus $^{31}\text{P}\%$, $^1\text{H}\%$ peaks (gray highlight) represent absolute ENDOR responses. *Insets*: (a) $^{31}\text{P}\%$ ENDOR responses of exemplars and eggs/embryos from frog 3; (b) corresponding $^1\text{H}\%$ ENDOR responses. (* is a ^{55}Mn ENDOR signal) **c**. ^{14}N 3-pulse ESEEM timewaves of: eggs (black); embryos (red), each multiplied by 5 for ease of comparison; solution Mn-imidazole complex (purple). *Experimental conditions*: see Supplemental Methods (**b**, **c**, Fields $\sim 12.5\text{ kG}$). In **a**, **b**, and **c**. $n = 3$ biologically

independent replicates of intact frog eggs and embryos examined over 3 independent experiments.

Author Manuscript

Author Manuscript

Author Manuscript

Author Manuscript

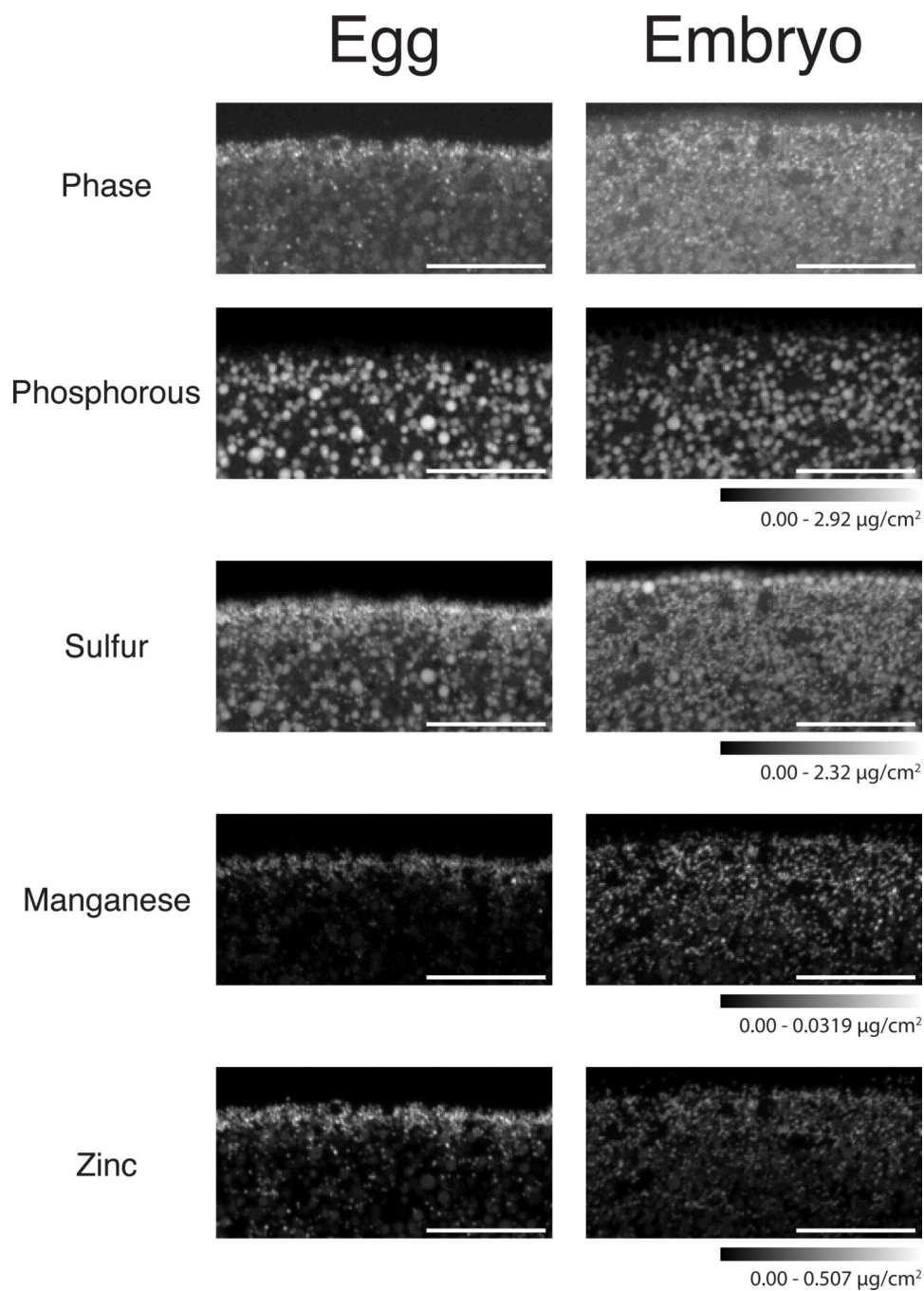
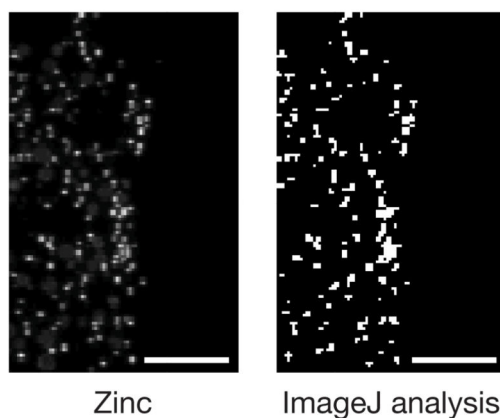
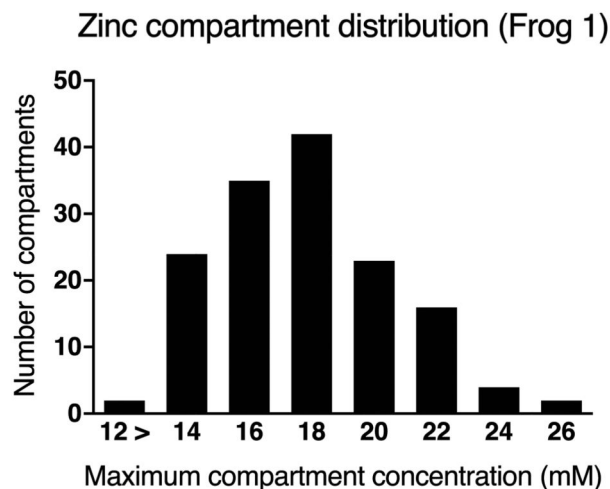


Figure 4: Synchrotron-based X-ray fluorescence mapping of egg and embryo cortices. X-ray fluorescence microscopy images of the animal pole of fixed *Xenopus* egg/embryo slices show zinc and manganese are localized in small cortical compartments. Scale bar = 20 μm . Images acquired at Beamline 2-ID-D at Argonne National Laboratory. Pixel size: 300 \times 300 nm, slice thickness: 2 μm , scan time: 500 ms/pixel. These are representative images of slices of eggs/embryos from 7 different frogs imaged over 3 experiments.

a

	Average $\mu\text{g}/\text{cm}^2$	Voxel Concentration (mM)
Mn	$4.0 \pm 1.1 \times 10^{-3}$	2 ± 0.5
Co	$5.9 \pm 6.7 \times 10^{-3}$	3 ± 3
Ni	$6.7 \pm 1.7 \times 10^{-4}$	0.3 ± 0.07
Cu	$2.4 \pm 1.5 \times 10^{-2}$	10 ± 6
Zn	$5.0 \pm 0.66 \times 10^{-2}$	20 ± 3

Mean \pm SD. n = 3 frogs**b****c****Figure 5: Animal pole egg metal compartment contents.**

Metals are stored at millimolar concentrations in the cortical compartments. **a.**

Concentrations of metal compartments in the egg animal pole. Voxel size $300 \times 300 \times 400$ nm. Data acquired at Beamline 2-ID-D, Argonne National Laboratory. Values reported as mean \pm SD, n = 3 slices of eggs analyzed from separate frogs examined over 2

independent experiments. **b.** Representative image of zinc distribution and thresholding of areas of high zinc concentration. Scale bar = 10 μm . Images acquired at Beamline 2-ID-D at Argonne National Laboratory. Pixel size: 300×300 nm, slice thickness: 400 nm, scan time: 500 ms/pixel. **c.** Representative plot of the zinc concentration distribution of small metal compartments found in a slice. n = 156 compartments.

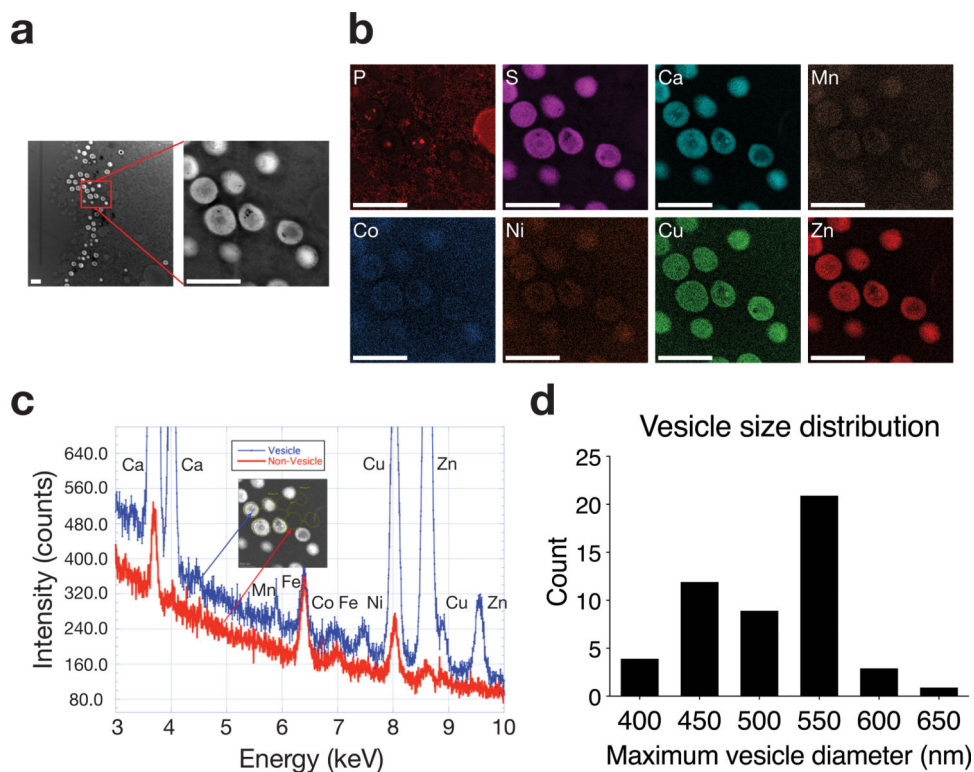


Figure 6: Analytical electron microscopic analysis of egg animal pole cortical vesicles. AEM demonstrates that multiple metals are stored in sub-micrometer vesicles in the animal pole. **a.** High Angle Annular Dark Field Scanning Transmission Electron Microscopy (HAADF-STEM) images of the cortex of the animal pole of a fixed *Xenopus* egg. **b.** Hyperspectral elemental intensity distribution maps: background corrected, with a 0.7-pixel gaussian blur, no normalization, no quantification. Same conditions as in **a.** Scale bar = 1 μm in both **a.** and **b.** These are representative images of 3 separate scans. **c.** Cumulative XEDS spectra confirming the presence of Ca, Mn, Co, Ni, Cu, and Zn in vesicles. These comparison spectra are obtained by summing individual spectra from an identical number of pixels in regions of interest which correspond to vesicle and neighboring non-vesicle areas. **d.** Histogram of vesicle diameter distribution from image in **a.** $n = 50$ vesicles measured.

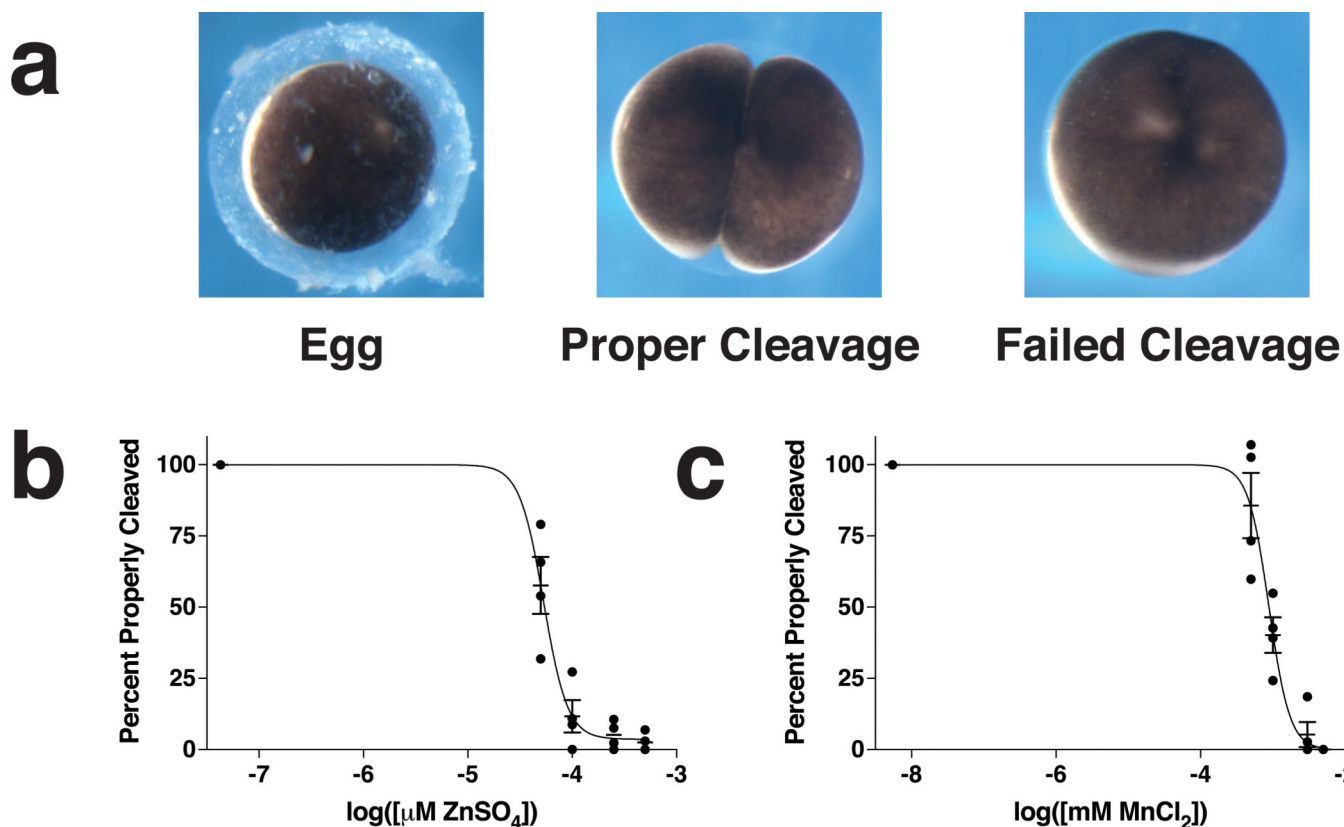


Figure 7: Extracellular zinc or manganese inhibits fertilization in a dose-dependent manner. Both extracellular zinc and manganese block fertilization. **a.** Images of an unfertilized *Xenopus* egg (in jelly coat), a properly dividing embryo (first cleavage), and an instance of failed cleavage (meiotic catastrophe). **b.** An IC_{50} graph of the effects of extracellular $ZnSO_4$ on the rate of fertilization. $IC_{50} = 53 \mu M$ (95% CI = 47 – 61 μM , $R^2 = 0.94$). Data are presented as mean percentage of eggs properly fertilized \pm SEM, $n = 4$ frogs (39 – 102 eggs per datapoint). See Supplemental Figure 11 for raw data. **c.** An IC_{50} graph of the effects of extracellular $MnCl_2$ on the rate of fertilization. $IC_{50} = 890 \mu M$ (95% CI = 770 μM – 1.0 mM, $R^2 = 0.93$). Data are presented as mean percentage of eggs properly fertilized \pm SEM, $n = 4$ frogs (36 – 100 eggs per datapoint). See Supplemental Figure 12 for raw data.